Instance-Level Microtubule Segmentation Using Recurrent Attention

Samira Masoudi^{1,2}, *Student Member, IEEE*, Afsaneh Razi¹, Cameron H.G. Wright², *Senior Member, IEEE*, Jay C. Gatlin², Ulas Bagci¹, *Senior Member, IEEE*

Abstract-We propose a new deep learning algorithm for multiple microtubule (MT) segmentation in time-lapse images using the recurrent attention. Segmentation results from each pair of succeeding frames are being fed into a Hungarian algorithm to assign correspondences among MTs to generate a distinct path through the frames. Based on the obtained trajectories, we calculate MT velocities. Results of this work is expected to help biologists to characterize MT behaviors as well as their potential interactions. To validate our technique, we first use the statistics derived from the real time-lapse series of MT gliding assays to produce a large set of simulated data. We employ this dataset to train our network and optimize its hyperparameters. Then, we utilize the trained model to initialize the network while learning about the real data. Our experimental results show that the proposed algorithm improves the precision for MT instance velocity estimation to 71.3% from the baseline result (29.3%). We also demonstrate how the injection of temporal information into our network can reduce the false negative rates from 67.8% (baseline) down to 28.7% (proposed).

Index Terms—TIRF microscopy, velocity tracking, multiple object tracking, instance-level segmentation, recurrent attention, MT-MT interaction.

I. INTRODUCTION

ICROTUBULES (MTs) are cytoskeletal polymers within eukaryotic cells composed of individual α -, β - tubulin subunits with head-to-tail arrangement. The inherent asymmetry of the heterodimeric subunits produces polar filaments with two distinct ends (one termed "plus" for the dynamic end and the other "minus for the more stable end) [1]-[3]. The polar structure of MTs and their highly regulated growth dynamics make them good candidates for many vital tasks in cellular level such as intracellular transportation, cell migration, polarization and the most critical one, cell division [2]. MTs are the primary components of mitotic spindle which is assembled by the cell to segregate the sister chromatids during cell division. Considering MTs' critical contribution to the maintenance of cell homeostasis and in cell division, it is not surprising that perturbations to MT function can lead to a wide range of diseases from cancer to neurodegenerative disorders [4]. Therefore, a quantitative analysis of MTs and the motors that arrange these filaments in space is important for understanding the underpinning mechanism of many diseases at the molecular level.

We dichotomize MTs' dynamics into two different levels:

- 1) Each single MT (with any mobility status: moving, immobile, etc.) undergoes several stochastic transitions between growth (subunit attachment), pause and shrinkage (subunit detachment) at its plus end [5]. This is called *dynamic instability*.
- 2) Multiple MTs move while interacting with their surroundings (particularly other MTs) through direct contact and/or by crosslinking via specific motor and non-motor proteins known as *microtubule associated proteins* (MAPs) [2], [6], [7].

While various investigations have focused on dynamic instability through tracking MT plus-ends [1], [2], the second dynamic type, i.e.,

changes in translation velocity due to interactions with motors, other proteins and MTs, is still an area that requires additional investigation. MTs move along and cross-link each other through motors and static, non-motile MAPs. The combined actions of these active and static MAPs spatially organize MTs relative to one another [8]. In the context of spindle assembly, there are two major classes of MT-based motor proteins that are explicitly important: dyneins and kinesins [9]. To assess the function of the respective MAPs and their potential contribution to MT sliding, MT interactions, and MT spatial arrangement, we develop the following strategy: to supply the required data for our analysis, herein we exploit the in-vitro MT motility assays to avoid the limitations caused by other intra-cellular processes. In these assays, we assemble the MTs in cell-free extracts derived from Xenopus laevis eggs [10] spiked with fluorescently labeled MAPs based on the Tau protein [11] that decorate MTs along their lengths. Endogenous cytoplasmic motors in the extract bind nonspecifically to the coverslip surface and power the observed MT gliding. The extract also contains a large complement of non-motor MAPs. The distance between the slide and the coverslip is 50 to 60 times greater than the 25nm MT diameter, providing sufficient space to enable multiple MTs to freely slide over each other.

We employ time-lapse total internal reflection fluorescence (TIRF) microscopy to visualize MT movements and dynamics [12], [13]. Inspired by kinematic properties of the observed MTs in our records. we create a prior indicating that sudden changes in MTs' velocity, in terms of direction and amplitude, are directly attributed to MT-MT interaction due to the MAPs existence. Figure 1 depicts such hypothesis in a smaller area of a real frame; A scenario where interaction between three MTs caused dramatic changes in their velocities. In this figure, velocity is computed regarding the head of the MT which moves forward and carries the rest of its body [14]. As it can be seen velocity variations are induced by changes in motion vector in terms of either amplitude (MT 3, blue vector in II and III), direction (MT 1, red vector in III and IV), or both (MT 1, red vector in II and III). Therefore, to chase the velocity trends of MT instances, we must track individual MTs in sequential frames. As demonstrated in Figure 1, multiple MTs tracking problem is challenging due to the following reasons:

- Low diversity in MTs' appearance,
- Time-varying nature of the features as a result of dynamic instability and photobleaching,
- Abrupt appearance/disappearance of MTs (pertaining to the use of TIRF microscopy which illuminates the upper 100nm distance between the slide and the coverslip) and,
- Unexpected changes in MTs' mobility patterns, ascribed to MTs' interaction and collision.

To address these challenges, we propose a solution composed of two distinct parts; Part 1: an instance-level MT segmentation is performed for each frame. Part 2: the segmentation results from single frames are fed into a data associating algorithm to develop a distinct path for each MT through the frames. Later, by exploiting the computed trajectories, MTs' velocity and displacement are estimated.

 $^{^{1}}$ Masoudi, Razi, and Bagci are with University of Central Florida, Orlando, 32816 FL.

²Masoudi, Wright, and Gatlin are with University of Wyoming, Laramie, 82071 WY.

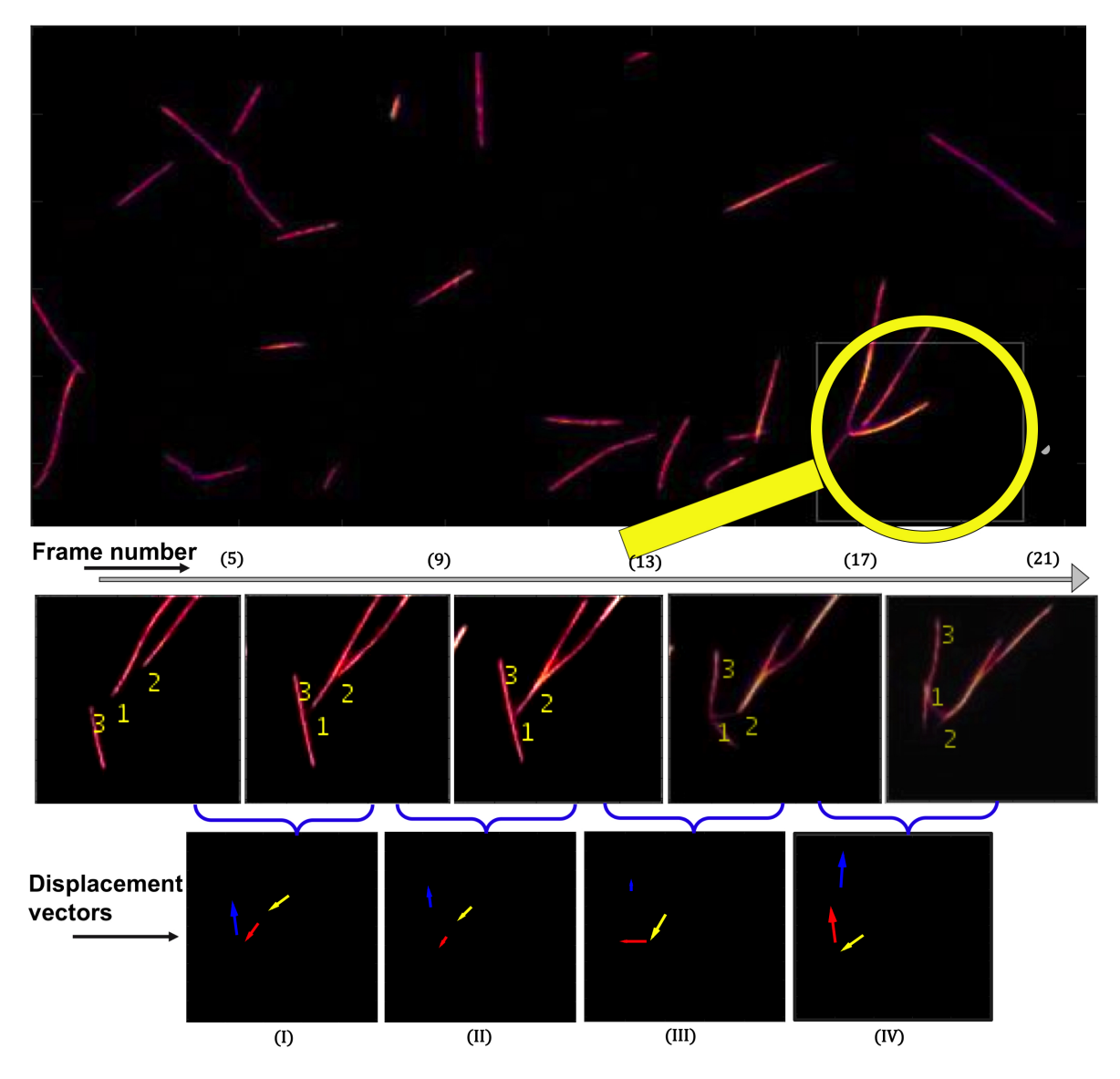


Fig. 1. A sample 256×512 real microscopy frame (first row), left to right sequence of its cropped version displayed with 4 frames per second sampling rate (second row), displacement labels of MTs 1, 2, 3 in red, yellow and blue respectively, between subsequent frames presented (third row).

Final results assist biologists to track the MTs' velocity trend through the frames, help to determine the potential MT-MT interactions, count the interactions in particular and know in what manner the density of MAPs existing in a volume, influences the rate of MT-MT interaction occurrence.

A. Related works

Early visualization of the MTs started with time-lapse images captured from fluorescently-labeled tubulin injected or expressed into the *living cells* [15], [16]. Application of this method was restricted to the cell periphery where sufficient density of MTs exist. To facilitate the *in vivo* exploration of dynamic instability, a considerable literature has grown up around utilizing the fluorescently labeled +TIPs that bind to the MTs plus ends. Parameters like MTs nucleation rate and growth speed were quantified by tracking the +TIPs using this method [9], [17], [18]. The computational analysis in this regard, was derived from multiple particle tracking algorithms. Literature splits the problem of multiple sub-cellular particle tracking into two steps of (1) recognition of the relevant objects and (2) associating the segmentation results. The individual performance of each of the detection

and the data association algorithms, working in concert to track MTs, directly affects the quality of the obtained spatiotemporal trajectories. Many particle detection (including localization) techniques have been discussed comprehensively in reviews [19], [20]. Prior works suggest to classify different segmentation procedures into thresholding, morphology-based, or Wavelet decomposition. Thresholding takes advantage of the moving objects being brighter than the static background in fluorescence microscopy images. In [14], a global threshold value was determined by using Otsu's Method whereas [21] applied entropy minimization for the same purpose. Other techniques have offered local thresholding or local maximum of a band-pass filter for segmentation. Morphology-based methods by contrast use the shape, as Top Hat [22], [23] or its 3-D version, Rolling Ball [24]. Works by [25], [26] established that wavelet decomposition also performs well in object detection. Either works decomposes an image into several levels and extracts a certain scale depending on the size of the desired particle. In this framework, the coarser and finer components represent the background and uncorrelated noise, respectively. Additionally, there are studies that use a combination of two or more of the aforementioned methods. In works such as [27]

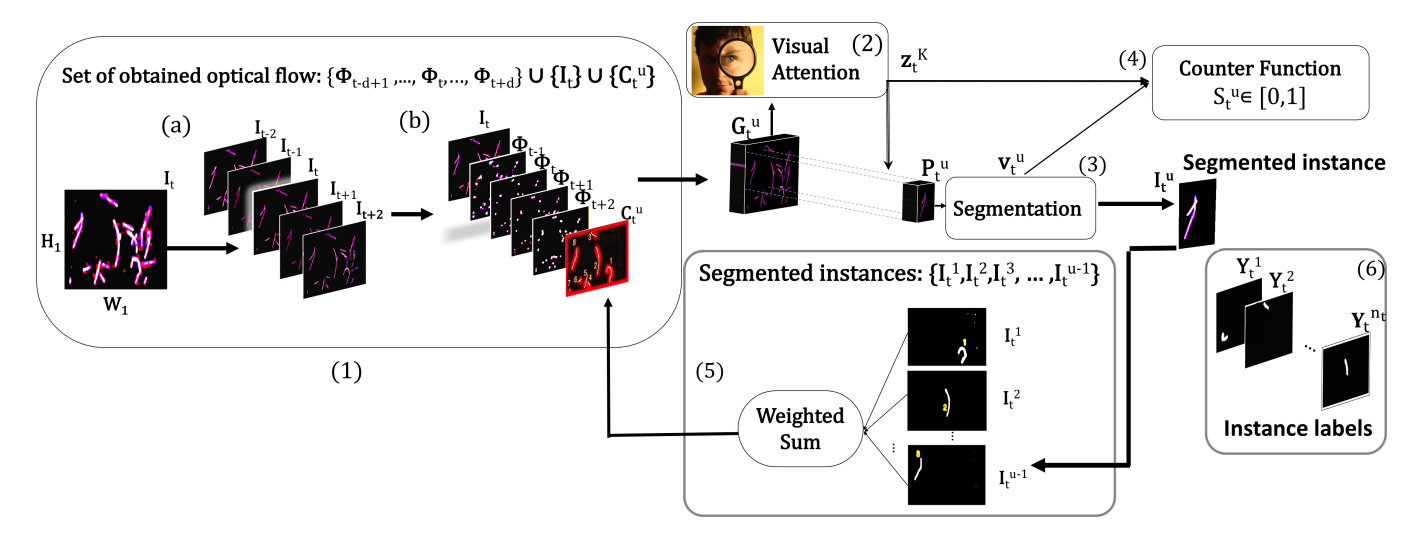


Fig. 2. General flowchart of the proposed method to segment MT instances. In (1) the original image \mathbf{I}_{t}^{u} and 2d number of its surrounding frames (a) reform to 2d optical flows. The set of the optical flows along with the original image and the already u-1 segmented instances at the current frame (\mathbf{C}_{t}^{u}), configure a group (b), to supply the input, (2) contains the visual attention which determines where in the image the network should look for the next instance, (3) segmentation recognizes an instance inside the subjected area, (4) scores the performance of attention and segmentation elements to return a verdict about the segmentation quality, if the score drops under a certain threshold, network stops iterating over the same image, resets itself and moves forward to \mathbf{I}_{t+1}^{u} , (5) collects the already segmented instances 1:u-1, linearly combine them and fed the result back to the input, (6) represents the layers of binary masks for individual MT labels.

or [18], authors used the watershed segmentation (thresholding and region growing algorithms) supported by Gaussian fit modeling to detect MTs in +TIP images. [19] used Gaussian denoising and benefited from both morphological and thresholding methods concurrently. However, any of these methods suffices segmentation in a sequence of time-lapse images for ultimate tracking purposes. That is due to the time-varying nature of the image intensities, caused by photobleaching, molecular-level processes or unique sub-cellular dynamics. A reasonable solution to overcome these difficulties could be normalization or background subtraction. Recent developments [28], [29] have also highlighted the more efficient parametric models to jointly estimate background and desired bright particles. [28] applied conditional Markov random field to model the local statistics and used the spatial correlations for his analysis.

Likewise, a search of the literature reveals several methods of data association between the segmentation results from individual frames. These optimization algorithms may concern two consecutive frames [27], [30], [31], multiple succeeding frames [32], [33] or a batch of frames with more complex graph pruning techniques [34], [35]. In assigning the segmented objects from individual frames to each other, several challenges emerge e.g. having a low SNR ratio in an image is a common issue that is cured by the application of probabilistic approaches [17], [36]. Even if adequate SNR is provided, attributing the detected particles, that suddenly appear/disappear, to their true trajectories in TIRF microscopy images is a real struggle. The instantaneous appearance/disappearance of the particles as well as the potential length changes can be mistaken for moving objects. High enough frame rate followed by proper post processing such as two-frame or frame difference assignment approaches can solve this issue. In some certain imaging types such as +TIPs imaging the incapability to reveal the pause or shrinkage phases of MTs necessitates extra processing discussed by [1], [18], [27]. The introduced *plusTipTracker* software package traces MTs plus ends while compensating for their missed phases [27]. Another major study [37] suggested a customized platform to catch up with photobleaching and photon-limited nature of images by employing a variance stabilization transform. The heterogeneous motion patterns

of various instances in multiple particle tracking is a challenging addition to all previously referred difficulties [35]. Interacting multiple model filtering, piecewise-stationary motion modeling and piecewise-stationary multiple motion Kalman smoother are the latest studies that incorporate the Bayesian prediction power to optimize the assignment [12], [14], [34], [35]. There is a complete literature review on the most common data association techniques in particle tracking applications by [38]. The results indicate that missing detections are far more problematic than imperfect detections to the data association performance. By avoiding misdetections (reducing the false negetives), there is no need to use sophisticated multi-frame linking techniques [38]. The most recent development in this area is the application of deep learning to the problem of data association in multiple particle tracking which has been addressed in [39].

The research gap: While previous studies attempted to measure descriptive parameters of dynamic instability, our project offers a fresh perspective toward MTs. In this work, we are specifically interested in translation velocity of MTs *in-vitro*, where they are exposed to frequent MT-MT interaction. Velocity estimation is realized through instance-level MT segmentation and tracking in turn. To outperform the preceding tracking algorithms, a pioneer segmentation approach with fewer false negatives is desired. This paper proposes a novel deep learning based methodology which helps us to avoid the shortcomings of manual feature extraction, reduces false negatives and false positives while tackling the motion complexity.

II. METHODS

A. Overview of the proposed method

Our method can be best described under two headings: Part 1) instance-level MT segmentation for each frame, Part 2) data association of MTs among frames. The first involves segmentation which gets extremely challenging when MTs *overlap* or *collide* in some scenarios. To address such overlapping problems, we present a new instance-level segmentation algorithm based on a recurrent neural network (RNN). Figure 2 shows the flowchart of our segmentation platform guided by a novel visual attention model that goes through each frame repeatedly, each time to segment a single MT.

The designed structure facilitates much more efficient delineation of individual MTs where a considerable number of MT-MT interactions occur. Briefly, Step 1 is the data preparation module: original image, a sequence of optical flows obtained from its neighboring frames, along with a weighted sum of the results from already segmented instances at the current image. Step 2 creates visual attention which processes the input data to propose where to focus for further inspection. Step 3 indicates the segmentation unit that attempts to detect one instance inside the suggested area. Step 4 is a scoring function that validates the segmented instance in Steps 2 and 3. This part is essential since it learns how to discern true instance segmentation to avoid iterating over false detections. In Step 5, the most recent segmented instance joins all the previously recognized instances from the same frame and all are fed back to the input. Later in Part 2, on obtaining the segmentation results from individual frames, for every pair of the succeeding frames, we take their segmented MT instances into a Hungarian algorithm.

As a consequence, we get trajectories of MTs along the frames that promote MT velocity estimation. To the best of our knowledge, this is the first study exploring the problem of MT segmentation and tracking with a deep learning algorithm. In order to evaluate the proposed design and optimize its hyperparameters, we first apply it to simulated data which imitates the actual time-lapse microscopy images of MTs. Based on a network trained using the simulated data, we employ the obtained weights to initialize the training procedure of the same structure on the real data.

B. Notations

Throughout this paper, we assume that our proposed configuration goes through sequential time-lapse images $I = \{I_1, I_2, ..., I_T\}$, each of which has a size of $H_1 \times W_1 \times 3$. We adopt n_t to denote the number of true MT instances at the t^{th} frame. Inevitable lower index t is used as the number of MTs existing in different frames may vary considerably.

In the first part of our method, given I, a set of the subsequent frames, we intend to segment all MTs at I_t . We use m_t to refer to the total number of detected instances at frame t. For this purpose, we use a recurrent attention-based instance-level segmentation approach. For the second part, obtaining m_t and m_{t+1} MT instances at each two succeeding frames, we associate the results to get three types of MT count at each frame: MTs exiting, or entering the current frame, and those transferring to the next frame.

C. Part 1: Instance-level MT segmentation in a single frame

Deep neural networks have shown an impressive performance in various vision tasks such as object recognition and image segmentation [40]–[42]. Yet their potential for instance segmentation has not been fully demonstrated in biomedical imaging. Our research is specifically focused on cases where multiple incidences of the same kind may occur at each frame in a sequence of images. Inspired by the recent computer vision applications by Ren et al. [40] and Hu et al. [43], we present a new system of attention to accurately segment an individual MT among the crowd of MTs. The attention module specifies where to look for the next instance. It uses Gaussian kernels to blur out the exterior and enhance the interior of the attention area in the input set. Next, the segmentation network extracts an instance of the MTs in the suggested region.

Our proposed strategy is to iterate multiple times through a desired frame to segment one instance at each repetition. To explain the details of our segmentation procedure, we assume our network is about to begin its u^{th} iteration at frame \mathbf{I}_t . Terms $\mathbf{G}_t{}^u$ and $\mathbf{I}_t{}^u$ respectively describe the input and the output of our algorithm at this iteration. With this assumption, the overall structure of our network takes the form of the following elements:

1) Input: For initial determination of motion vectors, we simply follow the work of Liu [44] to calculate a series of optical flows from the sequence of time-lapse images. Φ_t indicates the optical flow between a pair of consecutive frames $(\mathbf{I}_{t-1}, \mathbf{I}_t)$. We compute a set of 2d optical flows, $\Phi_{t,2d}$, using 2d+1 successive frames centered at \mathbf{I}_t . The obtained set of the optical flows $\Phi_{t,2d}$, original frame \mathbf{I}_t , along with the most updated \mathbf{C}_t^u as is defined in Step 5 by Eq. 8, arrange a group to supply the input:

$$\mathbf{G}_t^u = \{ \mathbf{\Phi}_{t,2d}, \mathbf{I}_t, \mathbf{C}_t^u \}. \tag{1}$$

2) Visual attention: The proposed attention network contains a CNN followed by a long-short term memory (LSTM). The goal is to localize the region of attention for a constrained segmentation. First, the CNN breaks down the $H_1 \times W_1$ input region into $H_2 \times W_2$ non-overlapping tiles, where $H_2 < H_1$ and $W_2 < W_1$. As an output, for each tile located at (h_2, w_2) , CNN generates an L-feature vector \mathbf{q}_t^{u,h_2,w_2} . Putting these feature vectors all together forms the tensor \mathbf{Q}_t^u with $H_2 \times W_2 \times L$ dimension as illustrated in Figure 3.

Later, the LSTM receives the \mathbf{Q}^u_t as an input and starts iterating to find those tiles that contribute the most to the attention region for the u^{th} instance. This region is assumed to be the smallest possible area containing an individual MT. With this aim, the LSTM produces matrix \mathbf{A}^k_t with size $\mathbf{H}_2 \times \mathbf{W}_2$, at its k^{th} repetition. Every entry in

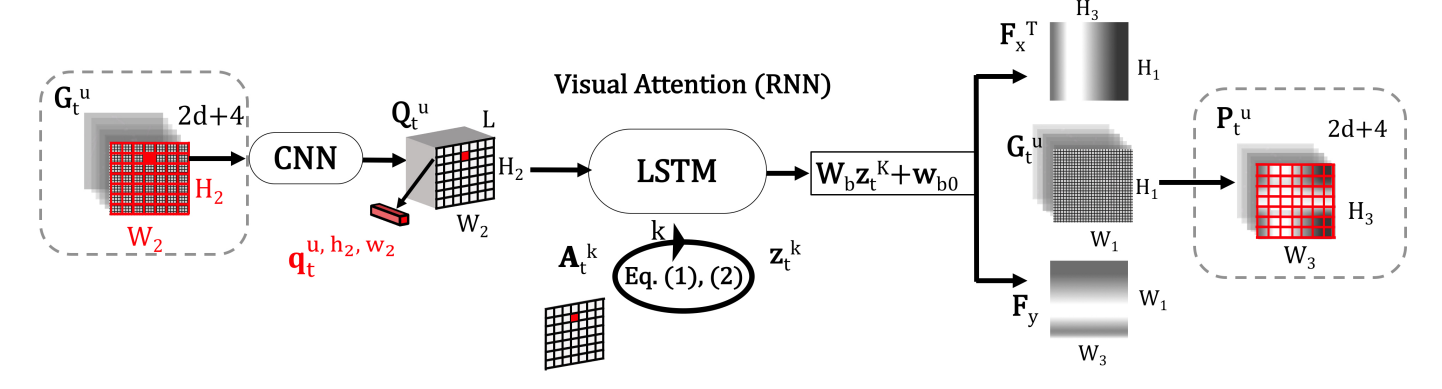


Fig. 3. Visual attention module: CNN produce an L-feature vector \mathbf{q}_t^{u,h_2,w_2} for each tile in the input group, LSTM iterates K times and assigns a contribution level $\mathbf{A}_t^k(h_2,w_2)$ to the respective tile at its k^{th} repetition, after convergence of the LSTM, its recent hidden state implies two vertical and horizontal Gaussian kernels. These kernels together propose the attention region.

this matrix expresses the level of contribution for its respective tile. The LSTM initiates with all tiles participating equally in the attention region but gradually fine-tunes along with the LSTM hidden state \mathbf{z}_t^k evolution, according to Eqs. 2 and 3.

$$\mathbf{A}_{t}^{k} = \begin{cases} 1/(\mathbf{H}_{2} \times \mathbf{W}_{2}), & \text{if } k = 0, \\ MLP(\mathbf{z}_{t}^{k}), & \text{otherwise,} \end{cases}$$
 (2)

in which MLP(.) denotes a multi-layer perceptron

$$\mathbf{z}_{t}^{k} = \begin{cases} 0, & \text{if } k = 0, \\ \text{LSTM}\left(\mathbf{z}_{t}^{k-1}, \sum_{h_{2}, w_{2}} \mathbf{A}_{t}^{k}(h_{2}, w_{2}) \mathbf{q}_{t}^{u, h_{2}, w_{2}} \right), & \text{otherwise.} \end{cases}$$
(3)

The LSTM keeps repeating up to the point where all the elements in \mathbf{A}_t^k converge. We refer to the last iteration number as K and use it as an upper index to specify the most updated hidden state \mathbf{z}_t^K . Using a linear transformation of the final hidden state \mathbf{z}_t^K , we compute the describing parameters of the attention region (Eq. 4). These parameters are the mean and the standard deviation of Gaussian kernels \mathbf{F}_x and \mathbf{F}_y along the x and y axes:

$$[\mu_x, \mu_y, \sigma_x, \sigma_y]^{\mathsf{T}} = \mathbf{W}_b \mathbf{z}_t^{\mathsf{K}} + \mathbf{w}_{b0}. \tag{4}$$

We apply Gaussian kernels to fulfill two tasks simultaneously: first to intensify the attention while attenuating the rest of the image, and to re-sample the $H_1 \times W_1$ area of the input group to $H_3 \times W_3$ in \mathbf{P}^u_t for amplified details inside the desired region ($H_3 < H_1$ and $W_3 < W_1$). We calculate Gaussian kernels \mathbf{F}_x and \mathbf{F}_y based on Eq. 5 to transform the input \mathbf{G}^u_t into the final attention region \mathbf{P}^u_t (Eq. 6). In other words, pixels from the original image contribute to each pixel in the attention region according to matrices \mathbf{F}_x and \mathbf{F}_y .

$$\mathbf{F}_{x}[h_{1}, h_{3}] = \frac{1}{\sigma_{x}\sqrt{2\pi}} \exp{-\frac{(h_{1} - \mu_{x})^{2}}{2\sigma_{x}^{2}}},$$

$$\mathbf{F}_{y}[w_{1}, w_{3}] = \frac{1}{\sigma_{y}\sqrt{2\pi}} \exp{-\frac{(w_{1} - \mu_{y})^{2}}{2\sigma_{y}^{2}}},$$
(5)

$$\mathbf{P}_t^u = \mathbf{F}_x^{\mathsf{T}} \mathbf{G}_t^u \mathbf{F}_u. \tag{6}$$

3) Segmentation: In order to segment the dominant object in the attention region, we apply a structure similar to what has been done by Noh et al [45]. As is shown in Figure 4, the back-to-back Encoder-Decoder design would turn the attention region \mathbf{P}_t^u into an R-feature vector \mathbf{v}_t^u first. It constructs a pixel-wise prediction map of the segmented instance $\hat{\mathbf{P}}_t^u$, after. To re-project back the segmentation result into a comparable size with the original image, it undoes the effect of the Gaussian kernels eventually.

$$\mathbf{v}_{t}^{u} = \operatorname{Encoder}(\mathbf{P}_{t}^{u}),$$

$$\hat{\mathbf{P}}_{t}^{u} = \operatorname{Decoder}(\mathbf{v}_{t}^{u}),$$

$$\mathbf{I}_{t}^{u} = \mathbf{F}_{x}\hat{\mathbf{P}}_{t}^{u}\mathbf{F}_{y}^{\top}.$$
(7)

4) Counter function: A critical addition to this architecture is the counter function which determines whether the attention region includes an instance or not. The counter function is made of a fully connected layer and a Sigmoid function. This module takes in a vector concatenating two vectors $\mathbf{z}_t^{\mathrm{K}}$ (the most updated RNN hidden state) and \mathbf{v}_t^u (encoder output) to generate a scalar value \mathbf{S}_t^u (see Figure 4). We train the weights in counter function so that the value of the \mathbf{S}_t^u lies in the interval of [0,1] with a higher score expressing more certainty toward the instance segmentation. As is depicted by Figure 4, counter function acts like a switch during the test. If \mathbf{S}_t^u surpasses a certain threshold, the network counts the segmented instance as a successful attempt and keeps iterating through the same

frame. Otherwise, an unqualified instance segmentation forces the network to stop iterating through the same frame, reset itself and step forward to the next frame along the time-lapse images.

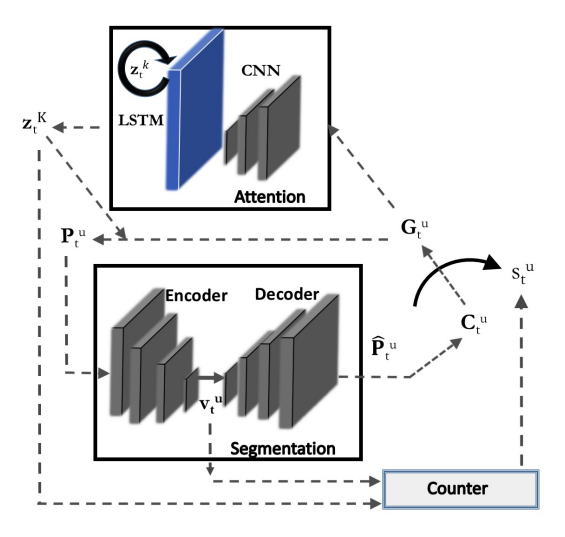


Fig. 4. Structural details of the deep network layers; counter resets the network to move froward to the next frame.

5) Feedback: Each segmented instance will join all previously segmented instances to be blended into the \mathbf{C}_t^u as part of the input set (Eq. 8). Feeding this weighted average into our network facilitates the segmentation of future instances in two ways: not only it causes smaller chance of selecting a region among the already assigned areas, it also provides a prior to the network based on the potential relation between various instances:

$$\mathbf{C}_{t}^{u} = \begin{cases} \mathbf{0}, & \text{if } u = 1, \\ \frac{1}{u-1} \sum_{i=1}^{j=u-1} \mathbf{I}_{t}^{j} & \text{if } u > 1. \end{cases}$$
 (8)

Training for segmentation: As described in above sections, our proposed algorithm, closely ties the segmentation and attention networks to each other. The attention network restricts segmentation to a certain area by locating the attention region using the results from former instance segmentation. However, level of dependency between these two networks are not equivalent. The segmentation performance is directly determined by the attention accuracy but segmentation results only provide extra guidance to the attention network. Such coupling forces us to implement the training procedure in two stages. First, we ignore the segmentation network and train the attention weights only and second, we train the whole network by fine-tuning the attention weights from former training stage while optimizing the segmentation weights from scratch. During the second stage, to prevent feeding the network with the premature segmentation results, we define a "knob" parameter. This parameter causes to feed back the ground truth into the network at the beginning and as the training progresses it gradually incorporates more products of the segmentation network instead. In any of these two training phases, we oblige our algorithm to iterate M times through each frame where M is determined by Eq. 9:

$$M = \max_{1 \le t \le T} \left(n_t \right) \tag{9}$$

This choice of M results in the algorithm learning about every instance in each frame but more it provides the opportunity for the counter function to learn about acceptable vs non-acceptable performance in instance-level segmentation. To account for the overlapped area at a single frame \mathbf{I}_t , we append multiple layers of binary ground truth masks \mathbf{Y}_t^u for all individual instances through their third

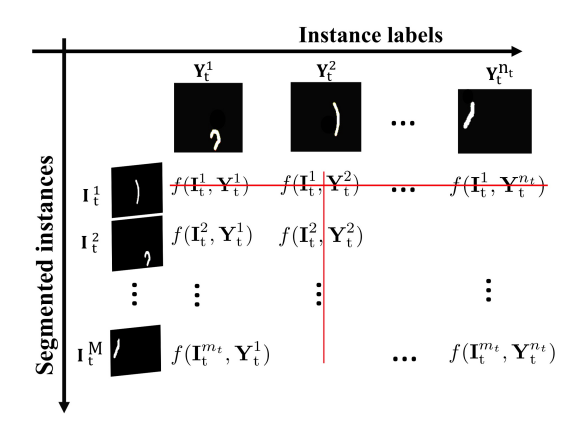


Fig. 5. The cost matrix of the Hungarian algorithm which measures the similarity between the segmented instances and instance labels (the higher values express more similarity).

dimension to form a 3-D label tensor \mathbf{Y}_t . Therefore, the network can learn about instances with conflicting areas that are either directly visible or hard to perceive due to occlusion. To compute the loss function we must evaluate the ground truth against our results. Since ground truth instances and resulted segmentations do not follow a unique order, we conduct M instance-level segmentation at a single frame first. A training-purpose Hungarian algorithm comes into play next. This algorithm optimally matches the results to the labels, based on a cost matrix as is depicted in Figure 5. We stipulate the cost function f in this figure as a measure of similarity between two matrices \mathbf{A} and \mathbf{B} of the same size:

$$f(\mathbf{A}, \mathbf{B}) = \frac{\sum (\mathbf{A} \circ \mathbf{B})}{\sum (\mathbf{A} + \mathbf{B} - \mathbf{A} \circ \mathbf{B})},$$
 (10)

where $\mathbf{A} \circ \mathbf{B}$ represents the Hadamard product and summation is performed over all the resulted entries. After forming the cost matrix, we employ the Hungarian algorithm to cross out the higher values as absolute matches first (such as \mathbf{Y}_t^2 and \mathbf{I}_t^1 in Figure 5) and optimize the rest of the matching procedure. As a result, we obtain a binary matrix which (i^{th}, j^{th}) element expresses if the i^{th} segmented instance (for any $i \in 1, ..., m_t$) corresponds to the j^{th} label, $(j \in 1, ..., n_t)$.

Loss function: To explain the loss function we use the terms defined in Table I at time t, for the i^{th} segmented instance and j^{th} label instance.

\mathbf{I}_t	Original frame								
$\mathbf{I}_t^{\mathrm{AR}_i}$	Binary mask of the obtained attention region $(\mathbf{F}_x \mathbf{P}_t^u \mathbf{F}_y^\top)$								
\mathbf{I}_t^i	Binary mask of the segmented instance								
S^i_t	Obtained score								
\mathbf{Y}_t	3-D matrix of binary labels								
$\mathbf{Y}_t^{\mathrm{AR}_j}$	Binary label of the attention region								
\mathbf{Y}_t^j	Binary label of instance								
$S_t^{j^*}$	True score								

The total loss L is defined as the sum of $L_{\rm att}$ (loss of the attention network), $L_{\rm seg}$ (loss of the segmentation network) and $L_{\rm count}$ (loss of the counter function):

$$L = L_{\text{att}} + L_{\text{seg}} + L_{\text{count}}. (11)$$

Based on the results attained from the training-purpose Hungarian algorithm, we define $L_{\rm att}$ as follow:

$$L_{\text{att}}(\mathbf{I}_t, \mathbf{Y}_t) = -\frac{1}{m_t} \sum_{i,j} l_{\text{att}}(AR_i, AR_j), \tag{12}$$

in which $l_{\text{att}}(AR_i, AR_j)$ is specified as in Eq. 13 to measure the similarity between the i^{th} proposed attention region and the j^{th} true detection box:

$$l_{\text{att}}(AR_i, AR_j) = \begin{cases} f(\mathbf{I}_t^{AR_i}, \mathbf{Y}_t^{AR_j}), & \text{if } i \text{ matches } j, \\ 0, & \text{otherwise.} \end{cases}$$
 (13)

Next component of the loss function is L_{seg}

$$L_{\text{seg}}(\mathbf{I}_t, \mathbf{Y}_t) = -\frac{1}{m_t} \sum_{i,j} l_{\text{seg}}(i,j).$$
 (14)

with $l_{\rm seg}(i,j)$ formulated as Eq. 15 to weight the similarity between i^{th} segmented instance and the j^{th} label instance:

$$l_{\text{seg}}(i,j) = \begin{cases} f(\mathbf{I}_t^i, \mathbf{Y}_t^j), & \text{if } i \text{ matches } j, \\ 0, & \text{otherwise.} \end{cases}$$
 (15)

There is also $L_{\rm count}$, for which we employ monotonic score loss as proposed by [40]. This definition compares the high scores with lower bound and vice versa, which makes the network to output more confident objects first.

$$l_{\text{count}}(\mathbf{I}_{t}, \mathbf{Y}_{t}) = \frac{1}{M} \sum_{i} -S_{t}^{i*} \min_{u \leq i} (S_{t}^{u}) - (1 - S_{t}^{i*})(1 - \max_{i \leq u} (S_{t}^{u}))$$
(16)

Inference for segmentation: During the test, our algorithm iterates over the test image and at the end of each iteration the final hidden state vector \mathbf{z}_t^K from the attention and \mathbf{v}_t^u vector from the segmentation result in a score by the counter function. If this score falls under a certain threshold, the counter function stops the algorithm from iterating through the same frame, resets the algorithm and goes to the next frame in the sequence of the time-lapse images.

D. Part 2: Data association

Once we got the results from individual frames, in the second part of our proposed solution, we associate the segmented instances for every two consecutive frames (t and t+1). For this purpose, we use an associating-purpose Hungarian algorithm with the cost function $f(\mathbf{I}_t^i, \mathbf{I}_{t+1}^j)$ to form the (i^{th}, j^{th}) element of the cost matrix. This function counts the *Intersection of Union* (IoU) between the i^{th} instance at time t and the j^{th} instance at t+1. Doing so, we obtain three types of MT counts during the test:

- $m_{t,t+1} \leq \min(m_t, m_{t+1})$ which is the number of instances that transfer to the next frame in a one-to-one manner.
- m_{t,ext} = m_t m_{t,t+1} indicating the number of instances at frame t which left the scene by either sudden disappearance or exiting the frame.
- $m_{t,ent} = m_t m_{t-1,t}$ which expresses the number of instances at frame t that enter the frame by a sudden appearance or simply move into the frame.

Any of these counts help to compute the displacement among segmented instances in successive frames.

III. RESULTS

A. Datasets

Here we have limited real data with annotations available, a common problem in biomedical imaging. Thus, we generate a type of data that closely simulates the actual microscopy images of MTs.

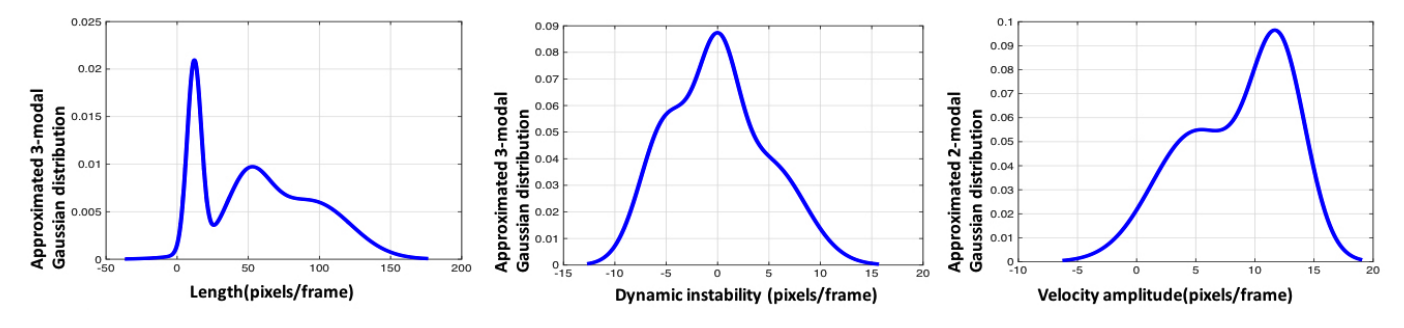


Fig. 6. Fitted PDF to the data obtained from 5000 randomly sampled individual MTs in real frames.

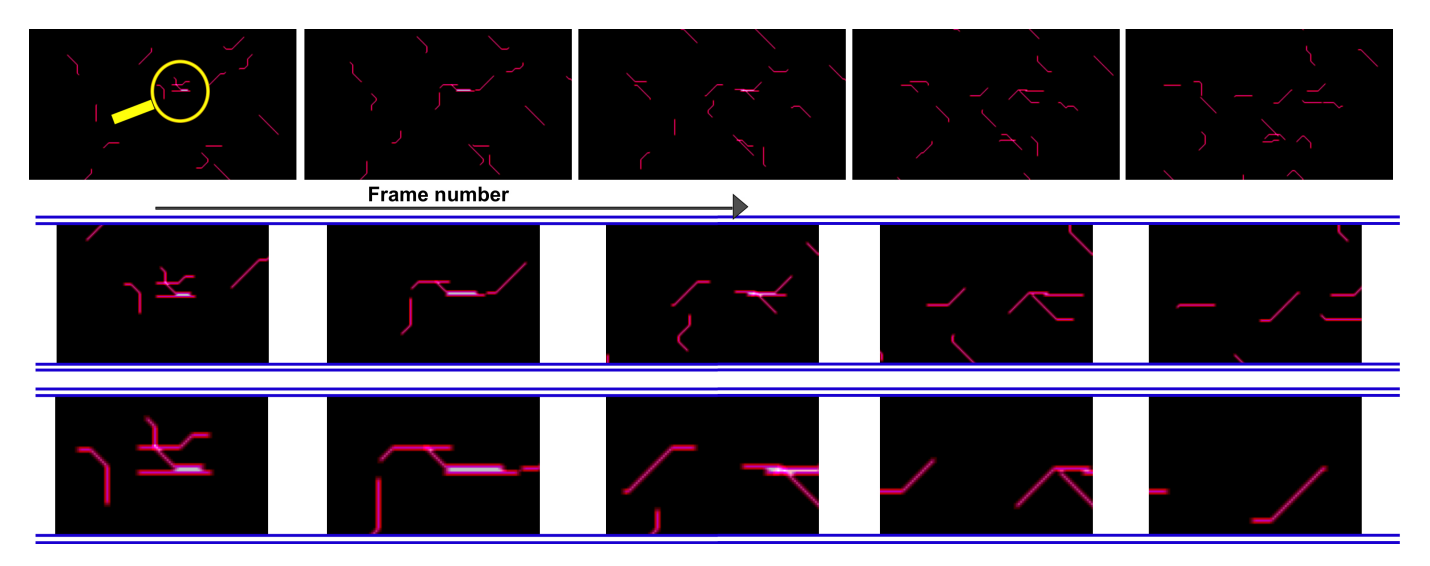


Fig. 7. left to right: temporally sub-sampled simulated data frames. First row includes original frames, second and third rows present their corresponding (2.5×2.5) and (5×5) zoomed versions (Color enhanced for better display).

a) Simulated data: Similar to the real time-lapse images, the simulated dataset should have RGB-channels captured from the central area of a large predefined frame to resemble the entrance and egress of the MTs on the edges. Specific settings to generate a simulated sequence of the images include: size and number of the frames, spatial and time resolution, initial number of the instances, their geometric specifications, and motion parameters. As it can be seen in Figure 7, MT instances are represented by wagon-trainshape structures with identical width. To better imitate the statistical characteristics of the real MTs such as their length, velocity, and dynamic instability, we collected respective information from real data. We took random samples of real instances with at least two experts having unanimous labels for them. We then fit a distribution to each relevant characteristic with the least mean square fitting error. The resulted distributions are displayed in Figure 6. In compilation of our simulated data, we make the MTs to take characteristics following the obtained distributions. Additionally, to mimic the TIRF microscopy another variable is taken into account indicating the sudden appearance/disappearance of the MTs. Besides, we utilize a contrast within our simulated image intensities where MTs have brighter interiors and even much lighter in their overlapping areas (see Figure 7). After generating the simulated data, we ignore the first few frames to avoid any bias induced by the initial conditions. All these details afford greater fidelity to the real-world microscopy images. In our study, we generate 20 simulated sequences, each containing 379 frames of size 256×256 pixels.

b) Real data: The real data contains 23 RGB, time-lapse sequences with the length of 23.16 ± 12.68 seconds. Each sequence

is sampled by 16 frames per second rate with 256×256 pixels spatial dimension. This dataset was annotated by a group of 3 experts. The experts were asked to click on five points along the length from head to tail of what they interpret as a single MT. Five is the smallest number that empirically shown to be enough for individual MT extraction from complex overlapping scenarios. These experts went through the whole time-lapse sequence to label a MT at a time which makes the obtained labels exempt from the data association step. Later, we use the 5-point labels to extract MTs bodies with further processing based on simple thresholding, region growing, and template matching algorithms [14]. Since there are some intravariations between the obtained labels, in each case we decide to use the most voted areas over all three labels as our ground truth in this paper.

B. Evaluation Metrics

The ultimate goal in this project is to estimate MTs' motions along sequential frames. We quantify the overall performance of our proposed method in terms of displacement estimation. It should be noted that displacement is measured with respect to relocation of MTs' heads. In the obtained trajectories, we subtract every two assigned instances at consecutive frames $(\mathbf{I}_{t+1} - \mathbf{I}_t)$ to have the area presenting the head of the MT. We use the center of this area and present it using (x^h, y^h) where h stands for head. Now we define displacement δ as in Eq. 17:

$$\boldsymbol{\delta} = [x_t^h \quad y_t^h \quad x_{t+1}^h \quad y_{t+1}^h]^T. \tag{17}$$

We compare δ to the ground truth (δ_{GT}) using a reformation of *Tanimoto index*, which we refer here as *Vsim*. Confirmed by Eq. 18, this measure evaluates the similarity between two displacements such that less angular difference and more equal magnitudes between two vectors result in greater *Vsim*:

$$Vsim(\boldsymbol{\delta}, \boldsymbol{\delta}_{GT}) = \frac{\boldsymbol{\delta}.\boldsymbol{\delta}_{GT}}{\left|\boldsymbol{\delta}\right|^2 + \left|\boldsymbol{\delta}_{GT}\right|^2} + \frac{1}{2}.$$
 (18)

Defining so, we identify the δ^* to find the best match for each of (δ_{GT}) 's among the resulted δ vectors:

$$\boldsymbol{\delta}^* = \underset{\boldsymbol{\delta}^i}{\text{arg max}} \left(\textit{Vsim}(\boldsymbol{\delta}^i, \boldsymbol{\delta}_{GT}) \right), \quad i \in \{1, ..., m_{t,t+1}\}.$$
 (19)

In this equations, we use δ^i for the i^{th} computed displacement. Next we calculate the best Vsim value itself and report it as an evaluating measure.

$$BVs = Vsim(\boldsymbol{\delta}^*, \boldsymbol{\delta}_{GT}). \tag{20}$$

After assigning each displacement to its equivalent ground truth, we count the true positives. We define true positive according to the intravariation existing between the three experts labeling outcomes, where we let our network to make errors less than the difference between the labels obtained from the experts. False positive is measured regarding the vectors that are not assigned to any ground truth or if assigned, they do not fulfill the requirements of being a true positive. We also define false negative considering the ground truth vectors to which, no estimated displacements are attributed. The average recall and precision are then determined. Difference in Counting (DiC) is the last metric we use to compare the counted number of segmented instances against the ground truths, in three formats:

$$|DiC|_{trans} = \frac{1}{T} \sum_{t} \frac{|m_{t,t+1} - n_{t,t+1}|}{n_{t,t+1}},$$

$$|DiC|_{ext} = \frac{1}{T} \sum_{t} \frac{|m_{t,ext} - n_{t,ext}|}{n_{t,ext}},$$

$$|DiC|_{ent} = \frac{1}{T} \sum_{t} \frac{|m_{t,ent} - n_{t,ent}|}{n_{t,ent}}.$$
(21)

C. Quantitative evaluations

Example results on the instance-level MT segmentation task are presented in Figure 8. As is shown in this figure, there is a significant positive correlation between the ground truth and results of our best model for both simulated and the real data. We analyze the performance of our algorithm in more details by providing three Tables II, III, and IV. All the available values in these tables are averaged over all the frames, all the instances (if applicable). Table II illustrates the distinction of our method against two baseline methods: adaptive template matching and Kalman smoother. The adaptive template matching stores a set of templates from the results in the optimum number of 5 past few frames [14]. Kalman smoother uses piece-wise stationary multiple motion model. As shown quantitatively in Table II, our framework outperforms the baseline results. A reduction of at least 0.235 in FP and 0.104 in FN prove the great capability of our method in dealing with complicated problem of multiple MTs segmentation and tracking.

Tables III and IV summarize the contrast between two possibilities of using raw frames and optical flow as part of the input. Results show that using optical flow can increase the precision up to 0.29 in case of the real data.

Ablation study: To unravel different characteristics of the proposed method, we design three different experiments, named Exp-1, Exp-2 and Exp-3. In Exp-1, we demonstrate how the injection of temporal

information into our instance-level segmentation network improves the quality of displacement estimation. We use various number of the frames to supply the network. Results in both Tables III and IV support the hypothesis of how a greater number of the frames leads to better estimations and less miss-detections (false negatives). Interestingly, using more frames does not improve the results necessarily. In our case, despite the huge computational burden using 7 number of the frames, it leads to an average BVs (i.e. measure of correct displacement estimation) of 0.458.

In Exp-2, we assess whether the temporal information affords better estimations in its raw form or optical flow. The results of this experiment is unrevealing by comparing Tables III and IV which shows a dramatic progress in case of using optical flow. Using optical flow adds an initial motion clue to the original image that pushes the network into a more accurate detection path. Theoretically we expect that providing the raw frames, an ideal network itself learns to extract similar information as optical flow. However, existing limitations caused to have advanced results using the obtained optical flow.

Finally, Exp3 is to study the network performance using simulated vs real data. Results from Tables III and IV confirm that the real data is harder to analyze. We get similarly higher results from our model comparing to the baseline methods for both data categories. Unlike our all-embracing labels for the simulated data (which includes the exact location of any pixel belonging to the target MT), we had only 5-marker coordinates directly annotated by the experts. This inevitable limitation is caused due to the limited time and expertise which significantly resolves the network's ability to segment the exact area. Nevertheless, this restriction does not prevent the network from its significant contribution to displacement estimation.

Overall, the manual segmentation and tracking of MTs to extract their displacements is a time consuming, error-prone procedure whereas the proposed algorithm in this paper can be a powerful substitute for human vision in doing such a task.

IV. DISCUSSIONS AND CONCLUDING REMARKS

Several methods have been proposed to track MTs +TIPs, however little is known about how to measure the translation velocity of MTs exposed to frequent MT-MT interaction. The nature of MTs motion vitiates either manual inspection or using any other simple modeling tools. Both human eyes and classic methods are biased by the population existing in a crowded scene. Switching patterns of MTs motion makes it even more challenging. It is also a time-consuming process for a specialist to go back and forth along the time-lapse images, focus on individual MTs and extract their velocities. All these limitations necessitate an automated approach with higher accuracy to accelerate the process of segmentation, tracking and analysis.

Here we employ new algorithm that iterates through attention and segmentation blocks to recognize one instance at a time. Our method demonstrates the benefits associated with deep neural networks: learning descriptive features of interest by itself where handcrafted attributes may fail. The attention network mimics the human vision to set the attention boundaries. Once attention proposed its candidate region, a back-to-back encoder-decoder segments the relevant instance inside this area. On completion of this process, a counter function evaluates both blocks in fulfilling an instance segmentation to rule about when to stop looking for a new instance. In another attempt, we inspect how temporal information may assist the velocity estimation. By taking a larger set of the neighbouring frames into account, we incorporate more information about the future and former position of the MTs. Temporal information also compensates for the unstable intensity of the MTs related to photobleaching. While too distant frames may provide misleading information for velocity estimation, the limited capacity of the designed structure also prevents

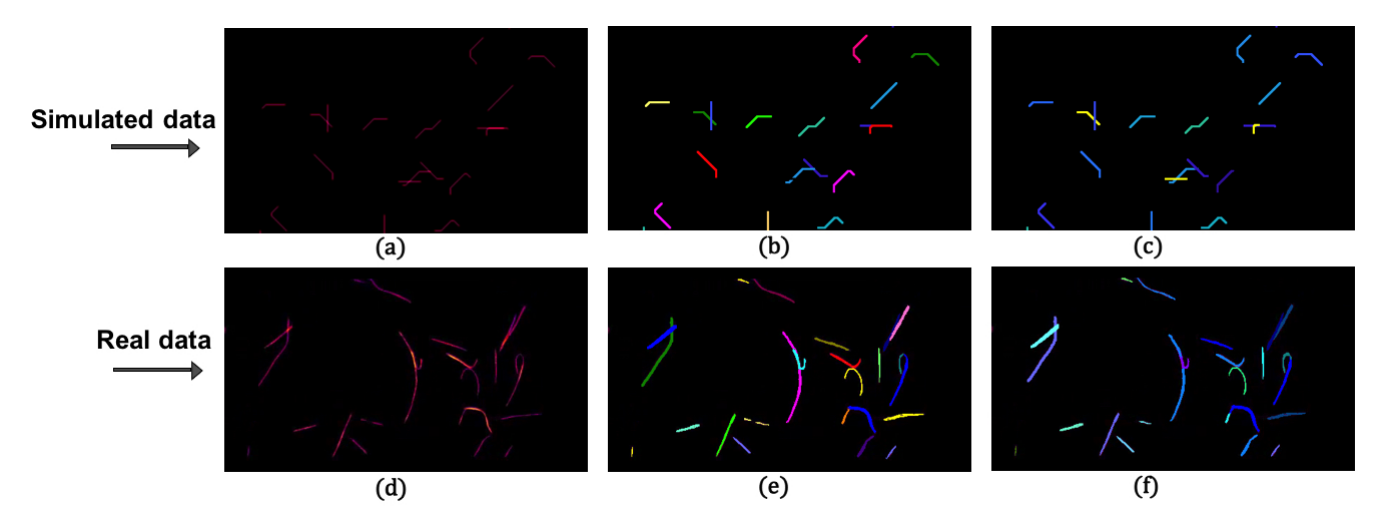


Fig. 8. Instance-level segmentation results, for simulated data (first row) and real data (second row). Columns show original frame, ground truth annotations and the results of the proposed method in order from left to right.

TABLE II

MULTIPLE MTS VELOCITY ESTIMATION PERFORMANCE IN TERMS OF BEST VSIM (**BVs**), FALSE POSITIVE (**FP**), FALSE NEGATIVE (**FN**),

PRECISION(**PR**), RECALL (**RE**) AND DIFFERENCE IN COUNTING (**DIC**).

	Dataset	BVs	FP	FN	Pr	Re	DiC	DIC_{ext}	DICent
Adaptive Template Matching [14]	Real	0.293	0.762	0.678	0.298	0.611	0.431	0.624	0.829
PMM Kalman Smoother [14]	Real	0.474	0.472	0.391	0.556	0.539	0.512	0.438	0.329
Ours (Optical Flow, WL=5)	Real	0.632	0.237	0.287	0.713	0.907	0.116	0.363	0.313

TABLE III MULTIPLE MTs velocity estimation using raw frames (threshold=0.23, WL = temporal window length).

	Dataset	BVs	FP	FN	Pr	Re	DiC	DICext	DICent
MMS(WL=1)	Sim	0.320	0.420	0.230	0.610	0.480	0.356	0.611	0.278
MMS(WL=3)	Sim	0.465	0.120	0.313	0.572	0.7410	0.273	0.454	0.438
MMS(WL=5)	Sim	0.665	0.001	0.149	0.624	0.926	0.118	0.413	0.404
MMS(WL=1)	Real	0.249	0.215	0.320	0.498	0.511	0.563	0.682	0.439
MMS(WL=3)	Real	0.544	0.327	0.319	0.487	0.543	0.542	0.512	0.418
MMS(WL=5)	Real	0.583	0.321	0.314	0.423	0.565	0.532	0.463	0.374

TABLE IV Multiple MTs velocity estimation using optical flow, (threshold=0.23, WL = temporal window length).

	Dataset	BVs	FP	FN	PR	RE	DIC	DIC_{ext}	DIC_{ent}
MMS(WL=3)	Sim	0.705	0.023	0.156	0.654	0.913	0.086	0.319	0.237
MMS(WL=5)	Sim	0.712	0.001	0.083	0.741	0.942	0.081	0.211	0.186
MMS(WL=3)	Real	0.588	0.268	0.151	0.646	0.889	0.171	0.390	0.349
MMS(WL=5)	Real	0.632	0.237	0.287	0.713	0.907	0.116	0.363	0.313

the network to learn much from these frames. In spite of the timeinsensitive essence of our algorithm during the training phase, it is reasonably useful for on-line tracking delayed by a few frames since it takes in, the future frames.

Regardless of the outstanding performance of our designed network, there still exist areas for continued development. Few available real labeled data is one of them. Adding a more realistic set of augmented data to our training dataset may significantly leverage the training quality. Conditional generative adversarial networks are potential platforms in this line of research [46]. Our proposed structure obeys human visual attention concerning instance-level segmentation in a single frame. It concentrates on different regions of a single frame and segments an instance in that region. Once all the results from individual frames are available, our algorithm associates the results to extract the trajectories. This structure can be extended into

a version that follows what an specialist practically does to track MTs in time-lapse images. That is, to segment an instance over all the frames and repeats this process for the rest of the instances. While our method prioritize spacial optimization to temporal smoothness, this latter approach emphasizes the temporal harmony. A well-designed architecture that could simultaneously incorporates both temporal and spacial dimensions of this problem is desired. Such structure bypasses the requirement for a following data association algorithm and generates results with additional spacial accuracy and temporal smoothness. As this research progresses, it is hoped that it will provide a better understanding of the underlying mechanics of cancer in the long term.

REFERENCES

[1] K. T. Applegate, Quantitative image analysis algorithms for the measurement of cytoskeleton dynamics. PhD thesis, The Scripps Research

- Institute, 2010.
- [2] T. Kreis and R. E. Vale, Guidebook to the Cytoskeletal and motor proteins, vol. 2. Oxford University Press, 1999.
- [3] J. Challoner, The Cell: A Visual Tour of the Building Block of Life. University of Chicago Press, 2015.
- [4] E. Harrison, "Medical news today." [Online]. Available: http://www.prezi.com/xz88yonibenc/the-malfunction-of-the-microtubules. [Accessed: 08- may- 2017].
- [5] T. Mitchison and M. Kirschner, "Dynamic instability of microtubule growth," *nature*, vol. 312, no. 5991, p. 237, 1984.
- [6] F. Pampaloni and E.-L. Florin, "Microtubule architecture: inspiration for novel carbon nanotube-based biomimetic materials," *Trends in biotech*nology, vol. 26, no. 6, pp. 302–310, 2008.
- [7] L. B. Pedersen and J. L. Rosenbaum, "Chapter two intraflagellar transport (IFT): role in ciliary assembly, resorption and signalling," *Current topics in developmental biology*, vol. 85, pp. 23–61, 2008.
- [8] C. E. Walczak and S. L. Shaw, "A map for bundling microtubules," *Cell*, vol. 142, no. 3, pp. 364–367, 2010.
- [9] J. C. Gatlin, A. Matov, A. C. Groen, D. J. Needleman, T. J. Maresca, G. Danuser, T. J. Mitchison, and E. Salmon, "Spindle fusion requires dynein-mediated sliding of oppositely oriented microtubules," *Current Biology*, vol. 19, no. 4, pp. 287–296, 2009.
- [10] A. Desai, S. Verma, T. J. Mitchison, and C. E. Walczak, "Kin i kinesins are microtubule-destabilizing enzymes," *Cell*, vol. 96, no. 1, pp. 69–78, 1999
- [11] P. Mooney, T. Sulerud, J. F. Pelletier, M. R. Dilsaver, M. Tomschik, C. Geisler, and J. C. Gatlin, "Tau-based fluorescent protein fusions to visualize microtubules," *Cytoskeleton*, vol. 74, no. 6, pp. 221–232, 2017.
- [12] I. Smal, I. Grigoriev, A. Akhmanova, W. J. Niessen, and E. Meijering, "Microtubule dynamics analysis using kymographs and variable-rate Particle filters," *IEEE Trans. Image. Process.*, vol. 19, no. 7, pp. 1861– 1876, 2010.
- [13] S. L. Shorte and F. E. Frischknecht, *Imaging cellular and molecular biological functions*. Springer Science & Business Media, Sep 2007.
- [14] S. Masoudi, C. H. G. Wright, N. Rahnavard, J. C. Gatlin, and J. S. Oakey, "Multiple microtubule tracking in microscopy time- lapse images using piecewise-stationary multiple motion model Kalman smoother," *Biomedical Sciences Instrumentation*, vol. 54, pp. 167–175, April 2018.
- [15] H. V. Goodson, J. S. Dzurisin, and P. Wadsworth, "Methods for expressing and analyzing GFP-tubulin and GFP-microtubule-associated proteins," *Cold Spring Harbor Protocols*, vol. 2010, no. 9, pp. pdb– top85, 2010.
- [16] I. Semenova and V. Rodionov, "Fluorescence microscopy of microtubules in cultured cells," *Microtubule Protocols*, pp. 93–102, 2007.
- [17] I. Smal, K. Draegestein, N. Galjart, W. Niessen, and E. Meijering, "Particle filtering for multiple object tracking in dynamic fluorescence microscopy images: Application to microtubule growth analysis," *IEEE Trans. Med. Imag.*, vol. 27, no. 6, pp. 789–804, 2008.
- [18] A. Matov, K. Applegate, P. Kumar, C. Thoma, W. Krek, G. Danuser, and T. Wittmann, "Analysis of microtubule dynamic instability using a plus-end growth marker," *Nature methods*, vol. 7, no. 9, p. 761, 2010.
- [19] I. Smal, M. Loog, W. Niessen, and E. Meijering, "Quantitative comparison of spot detection methods in fluorescence microscopy," *IEEE Trans. Med. Imag.*, vol. 29, no. 2, pp. 282–301, 2010.
- [20] M. K. Cheezum, W. F. Walker, and W. H. Guilford, "Quantitative comparison of algorithms for tracking single fluorescent particles," *Biophysical journal*, vol. 81, no. 4, pp. 2378–2388, 2001.
- [21] C. Kervrann, C. Ó. S. Sorzano, S. T. Acton, J.-C. Olivo-Marin, and M. Unser, "A guided tour of selected image processing and analysis methods for fluorescence and electron microscopy," *IEEE Journal of Selected Topics in Signal Processing*, vol. 10, no. 1, pp. 6–30, 2016.
- [22] F. Meyer, "Contrast feature extraction. quantitative analysis of microstructures in material sciences, biology and medicine," Special issue of Practical Metallography, Riederer Verlag, 1978.
- [23] E. J. Breen, G. H. Joss, and K. L. Williams, "Locating objects of interest within biological images: The Top Hat box filter," *J Comput-Assist Microsc*, vol. 3, pp. 97–102, 1991.
- [24] S. R. Sternberg, "Biomedical image processing," Computer, no. 1, pp. 22–34, 1983.
- [25] B. Zhang, M. Fadili, J.-L. Starck, and J.-C. Olivo-Marin, "Multiscale variance-stabilizing transform for mixed-poisson-gaussian processes and its applications in bioimaging," in Proc. Conf. ICIP, vol. 6, pp. VI–233, 2007.
- [26] J.-C. Olivo-Marin, "Extraction of spots in biological images using multiscale products," *Pattern recognition*, vol. 35, no. 9, pp. 1989–1996, 2002.

- [27] K. Jaqaman, D. Loerke, M. Mettlen, H. Kuwata, S. Grinstein, S. L. Schmid, and G. Danuser, "Robust single-particle tracking in live-cell time-lapse sequences," *Nature methods*, vol. 5, no. 8, pp. 695–702, 2008.
- [28] T. Pécot, P. Bouthemy, J. Boulanger, A. Chessel, S. Bardin, J. Salamero, and C. Kervrann, "Background fluorescence estimation and vesicle segmentation in live cell imaging with conditional random fields," *IEEE Trans. Image. Process.*, vol. 24, no. 2, pp. 667–680, 2015.
- [29] J. Boulanger, C. Kervrann, and P. Bouthemy, "Estimation of dynamic background for fluorescence video-microscopy.," in Proc. Conf. ICIP, pp. 2509–2512, 2006.
- [30] A. Sergé, N. Bertaux, H. Rigneault, and D. Marguet, "Dynamic multiple-target tracing to probe spatiotemporal cartography of cell membranes," *Nature methods*, vol. 5, no. 8, p. 687, 2008.
- [31] W. J. Godinez and K. Rohr, "Tracking multiple particles in fluorescence time-lapse microscopy images via probabilistic data association," *IEEE Trans. Med. Imag.*, vol. 34, no. 2, pp. 415–432, 2015.
- [32] N. Chenouard, I. Bloch, and J.-C. Olivo-Marin, "Multiple hypothesis tracking for cluttered biological image sequences," *IEEE Trans. on* pattern analysis and machine intelligence, vol. 35, no. 11, pp. 2736– 3750, 2013.
- [33] A. Jaiswal, W. J. Godinez, R. Eils, M. J. Lehmann, and K. Rohr, "Tracking virus particles in fluorescence microscopy images using multi-scale detection and multi-frame association," *IEEE Trans. Image. Process.*, vol. 24, no. 11, pp. 4122–4136, 2015.
- [34] V. Racine, A. Hertzog, J. Jouanneau, J. Salamero, C. Kervrann, and J.-B. Sibarita, "Multiple-target tracking of 3d fluorescent objects based on simulated annealing," *In Proc. Conf. ISBI: Nano to Macro*, pp. 1020–1023, 2006.
- [35] P. Roudot, L. Ding, K. Jaqaman, C. Kervrann, and G. Danuser, "Piecewise-stationary motion modeling and iterative smoothing to track heterogeneous particle motions in dense environments," *IEEE Trans. Image. Process.*, 2017.
- [36] W. J. Godinez, M. Lampe, R. Eils, B. Müller, and K. Rohr, "Tracking multiple particles in fluorescence microscopy images via probabilistic data association," *In Proc. Conf. ISBI: From Nano to Macro*, pp. 1925– 1928, 2011.
- [37] J. Boulanger, A. Gidon, C. Kervran, and J. Salamero, "A patch-based method for repetitive and transient event detection in fluorescence imaging," *PloS one*, vol. 5, no. 10, p. e13190, 2010.
- [38] I. Smal and E. Meijering, "Quantitative comparison of multiframe data association techniques for particle tracking in time-lapse fluorescence microscopy," *Med. Image. analysis*, vol. 24, no. 1, pp. 163–189, 2015.
- [39] Y. Yao, I. Smal, and E. Meijering, "Deep neural networks for data association in particle tracking," In Proc. Conf. ISBI, pp. 458–461, 2018.
- [40] M. Ren and R. S. Zemel, "End-to-end instance segmentation with recurrent attention," In Proc. Conf. CVPR, pp. 21–26, 2017.
- [41] A. Mortazi, R. Karim, K. Rhode, J. Burt, and U. Bagci, "Cardiacnet: Segmentation of left atrium and proximal pulmonary veins from mri using multi-view cnn," *In Proc. Conf. MICCAI*, pp. 377–385, 2017.
- [42] N. Torosdagli, D. K. Liberton, P. Verma, M. Sincan, J. S. Lee, and U. Bagci, "Deep geodesic learning for segmentation and anatomical landmarking," *IEEE Trans. Med. Imag.*, 2018.
- [43] Y.-T. Hu, J.-B. Huang, and A. Schwing, "Maskrnn: Instance level video object segmentation," In Proc. Conf. NPIS, pp. 325–334, 2017.
- [44] C. Liu et al., Beyond pixels: exploring new representations and applications for motion analysis. PhD thesis, Massachusetts Institute of Technology, 2009.
- [45] H. Noh, S. Hong, and B. Han, "Learning deconvolution network for semantic segmentation," in *Proceedings of the IEEE international con*ference on computer vision, pp. 1520–1528, 2015.
- [46] M. Chuquicusma, S. Hussein, J. Burt, and U. Bagci, "How to fool radiologists with generative adversarial networks? a visual turing test for lung cancer diagnosis," *In Proc. Conf. ISBI*, pp. 240–244, 2018.